IEEE TRANSACTIONS ON
PLASMA
SCIENCE

IEEE Xplore® Digital Library
http://ieeexplore.ieee.org/Xplore

Emittance Growth in the DARHT-II Linear Induction Accelerator

Carl Ekdahl, *Fellow, IEEE*, Carl A. Carlson, Daniel K. Frayer, B. Trent McCuistian, Christopher B. Mostrom, Martin E. Schulze, and Carsten H. Thoma

***Abstract*— The Dual-Axis Radiographic Hydrodynamic Test (DARHT) facility uses bremsstrahlung radiation source spots produced by the focused electron beams from two linear induction accelerators (LIAs) to radiograph large hydrodynamic experiments driven by high explosives. Radiographic resolution is determined by the size of the source spot, and beam emittance is the ultimate limitation to spot size. On the DARHT-II LIA we measure an emittance higher than predicted by theoretical simulations, and even though this accelerator produces sub-millimeter source spots, we are exploring ways to improve the emittance. Some of the possible causes for the discrepancy have been investigated using PIC codes. The simulations establish that the most likely source of emittance growth is a mismatch of the beam to the magnetic transport, which can cause beam halo.**

***Index Terms*— Linear induction accelerators, intense relativistic electron beams, beam instabilities, emittance.**

I. Introduction

FLASH radiography of hydrodynamic experiments driven by high explosives is a well-known diagnostic technique in use at many laboratories [1, 2]. At Los Alamos, the Dual-Axis Radiographic Hydrodynamic Test (DARHT) facility provides multiple flash radiographs from different directions of an experiment. Two linear induction electron accelerators (LIAs) make the bremsstrahlung radiographic source spots for orthogonal views. The 2-kA, 20-MeV DARHT-I LIA creates a single 60-ns radiography pulse [3]. The 1.7-kA, 16.5-MeV DARHT-II creates multiple radiography pulses by kicking them out of the 1600-ns long pulse accelerated by the LIA [4, 5, 6].

Beam emittance is the ultimate limitation on radiographic source spot size. In the absence of beam-target interaction effects, the spot size is directly proportional to the emittance. Since radiographic resolution is limited by the spot size, minimizing emittance enhances resolution of the radiographs. Therefore, investigation and mitigation of factors leading to high emittance beams is a worthwhile path to improving radiography.

Spot-size can also be enlarged by beam motion blur. Improvements in tuning the multi-pulse DARHT-II LIA have reduced the low-frequency inter-pulse beam motion to less than 1-mm at the accelerator exit [4]. Moreover, high-frequency motion due to the beam breakup (BBU) instability has been suppressed to less than 0.1 mm at the LIA exit [5]. However, concerns about beam emittance growth have yet to be addressed. Although no measurements of the emittance of the beam produced by the diode are available, detailed diode simulations with particle-in-cell (PIC) and particle-gun ray-trace codes predict a ∼200-300 π-mm-mr initial normalized emittance [5, 7]. On the other hand, measurements of emittance in the downstream transport (DST) imply an emittance $\geq 800\pi$-mm-mr after transport and acceleration through the LIA.

Three possibilities for this discrepancy are; our modeling of the diode is imperfect, the beam is perturbed soon after injection, or there is emittance growth in the accelerator or in the transport between the LIA and the measurement location. For the present article, we only investigate the possibility of emittance growth in the LIA.

In addition to beam instabilities, there are at least five readily identifiable macroscopic mechanisms for emittance growth in an LIA:

- Spherical aberrations of the focusing solenoids
- Large, helical beam trajectories.
- Strong dipole magnetic fields.
- Envelope oscillations.
- Non-uniform current distribution

These five mechanisms for emittance growth are amenable to investigation with particle-in-cell (PIC) simulations. A PIC code was used to simulate the beam in the DARHT-II LIA, with particular attention to these mechanisms for emittance growth. Emittance growth due to chromatic aberration is automatically included in all of the simulations, since the PIC code includes all space-charge effects, such as the beam energy spread due to space-charge depression. The results of these simulations and their implications for DARHT are the subject of this article. Section II describes the simulation codes used, and Section III discusses the PIC simulations and results.

II. Simulation Codes

Two simulation codes were used to explore the causes of emittance growth in DARHT-II: the XTR envelope code and the LSP-slice PIC code. These are described in the next two subsections.

Submitted for review on April 27, 2017. This work was supported by the National Nuclear Security Administration of the U. S. Department of Energy under contract number DE-AC52-06NA25396.

C. A. Ekdahl is with the Los Alamos National Laboratory, Los Alamos, NM 87545 USA (e-mail: cekdahl@lanl.gov).

B. T. McCuistian and M. E. Schulze are with the Los Alamos National Laboratory, Los Alamos, NM 87545 USA.

C. A. Carlson and D. K. Frayer are with National Security Technologies, Los Alamos, NM 87544 USA.

C. B. Mostrom and C. H. Thoma are with Voss Scientific, Albuquerque, NM 87108, USA.

Digital Object Identifier: 10.1109/TPS.2017.2755861

A. Envelope Codes

Design of tunes for the DARHT accelerators is accomplished using envelope codes. The two most frequently used are XTR [8] and LAMDA (Linear Accelerator Model for DARHT) [9]. In both of these codes the radius of a uniform density beam is calculated from an envelope equation [10, 11, 12]. In the DARHT accelerators the beam is born at the cathode with no kinetic angular momentum. Moreover, a reverse polarity solenoid is used to cancel out the magnetic flux through the cathode so that the canonical angular momentum of the beam is zero. The envelope equation for such a beam is

$$\frac{d^2r}{dz^2} = -\frac{1}{\beta^2\gamma}\frac{d\gamma}{dz}\frac{dr}{dz} - \frac{1}{2\beta^2\gamma}\frac{d^2\gamma}{dz^2}r - k_\beta^2 r + \frac{K}{r} + \frac{\varepsilon^2}{r^3}. \quad (1)$$

It can be shown that this same equation holds true for any axisymmetric distribution [9], so long as the radius of the equivalent uniform beam is related to the rms radius of the actual distribution by $r = \sqrt{2}R_{rms}$. Here, $\beta = v_e/c$, and $\gamma = 1/\sqrt{1-\beta^2}$, are the usual relativistic parameters. The beam electron kinetic energy is $KE = (\gamma - 1)\,m_e c^2$, the betatron wavelength is

$$k_\beta = \frac{2\pi\, B_z}{\mu_0 I_A}, \quad (2)$$

where $I_A = 17.08\beta\gamma$ kA, and the generalized perveance is $K = 2I_b/\beta^2\gamma^2 I_A$. The emittance which appears in Eq. (1) is

$$\varepsilon = 2\sqrt{\langle r^2\rangle\left[\langle r'^2\rangle + \langle (v_\theta/\beta c)^2\rangle\right] - \langle rr'\rangle^2 - \langle r v_\theta/\beta c\rangle^2}, \quad (3)$$

which is related to the normalized emittance by $\varepsilon_n = \beta\gamma\,\varepsilon$.

In a solenoidal focusing system as in DARHT-II the canonical angular momentum is conserved (Buch's theorem). The DARHT beams are born at the cathode with no mechanical angular momentum. Furthermore, the field angular momentum is zeroed there by using an opposite polarity solenoid to null the magnetic flux linking the cathode. Therefore, in the axial field of the solenoidal transport, the beam must rotate to conserve momentum, and for a uniform current distribution the beam rotates rigidly. For a rigidly rotating beam, the terms involving v_θ cancel, leaving simply

$$\varepsilon_n = 2\beta\gamma\sqrt{\langle r^2\rangle\langle r'^2\rangle - \langle rr'\rangle^2}. \quad (4)$$

In the azimuthal symmetry assumed in deriving Eq. (1), $\langle r^2\rangle = \langle x^2\rangle + \langle y^2\rangle = 2\langle x^2\rangle$ with similar expressions for the beam convergence and cross terms, so Eq. (4) reduces to

$$\varepsilon_n = 4\beta\gamma\sqrt{\langle x^2\rangle\langle x'^2\rangle - \langle xx'\rangle^2}, \quad (5)$$

which is the normalized Lapostolle "4-rms" emittance [13].

If all forces acting on the beam are linear with radius, the normalized emittance is theoretically expected to be invariant through the LIA. Since the beam self-forces due to a non-uniform current distribution are nonlinear, the invariance is invalid for such a beam. However, the XTR and LAMDA codes assume a uniform beam, and that the normalized emittance given by Eq. (3) is a constant through the LIA.

As described in [5], the initial conditions for solving the envelope equation are derived from simulations of the diode using the Trak ray-trace gun design code [14, 15]. The Trak calculations agree with particle-in-cell (PIC) simulations of the diode using the Large Scale Plasma (LSP) code [16]. The results of the two codes are in agreement, predicting a normalized emittance out of the diode in the range of 200 – 300 π-mm-mr.

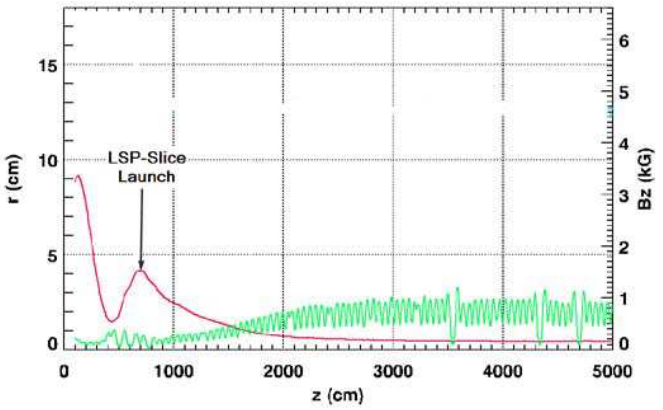

Fig. 1. Envelope code simulation of beam transport through the injector cell block and into the main LIA. (Green) The solenoidal focusing magnetic field strength on axis (scale on right). (Red) The beam envelope radius (scale on left).

The simple envelope equation in Eq. (1) is further improved in XTR as follows [17]. The energy dependence of the beam due to the gaps is approximated by a linear increase in γ accompanied by a thin-einzel-lens focus. Between gaps the value of γ used in Eq. (1) is the value at the beam edge, which is space-charge depressed by $\Delta\Phi \approx 30 I_b(2\ln R_w/r)$, where R_w is the radius of the beam pipe. XTR also uses the magnetic field at the beam edge, including a first order approximation to account for the flux excluded by a beam rigidly rotating in the magnetic field due to the invariance of canonical angular momentum [18].

The XTR code is used to design tunes for the DARHT–II LIA. The envelope equation integrations in XTR are initiated at the exit of the diode, with initial conditions provided by Trak code simulations of the diode. The beam envelope calculated by XTR for the nominal tune used for the simulations in this article is plotted in Fig. 1. The initial envelope focusing is the result of tuning the six injector cells (z<500 cm) to prevent beam spill at any energy from the beam head, which slowly rises from zero to ~2.2 MeV at the diode exit in ~500 ns. The beam envelope then rebounds through a focusing lattice with apertures designed to scrape off much of that off-energy beam head. This region is referred to as the Beam-head Clean-Up Zone (BCUZ). The beam is then refocused into the main LIA.

B. Particle-in-Cell Codes

The LSP-slice algorithm is based on the LSP PIC code [19]. A slice of beam particles located at an incident plane of constant z are initialized on a 2D transverse Cartesian (x, y) grid. The use of a Cartesian grid admits non-axisymmetric solutions, including beams that are off axis. Simulations were performed on a workstation with 32 processors. Multiprocessing reduced

the time for a typical run from the more than 30 hours required for earlier single processor runs to less than 4 hours. For axisymmetric beams, one can use a faster version of the code based on a 1D cylindrical grid. Using all 32 processors, the typical 1D run completes in less than 4 minutes. Excellent agreement between the 2D and 1D results have been obtained in comparison tests.

Initial electro- and magneto-static solutions are performed prior to the first particle push to establish the self-fields of the beam, including the diamagnetic field if the beam is rotating. After this initialization step, Maxwell's equations are solved on the transverse grid with $\partial/\partial z = 0$, and then the particles are pushed by the full Lorentz equations. At each time-step the grid is assumed to be located at the axial center-of-mass of the slice particles $z(t)$, which is propagating in the z direction.

The initial particle distribution of the slice is extracted from a full x, y, z LSP simulation. The distribution is a uniform rigid rotor with additional random transverse velocity. The rotation is consistent with zero canonical angular momentum in the given solenoidal magnetic field at the launch position. The random transverse velocity is consistent with the specified emittance. Best agreement between LSP-slice and full LSP 2D simulations was obtained when the slice model is initiated at an envelope extreme, where the beam convergence is zero, so this condition was used for all simulations for this article. Also, for this article, 2D simulations used 70,688 particles, and 1D simulations used 4,000 particles.

External fields are input as functions of z, and are applied at the instantaneous axial center-of-mass location. External fields that are azimuthally symmetric (fields from solenoids and gaps) are input as on-axis values, and the off-axis components are calculated up to sixth order using a power series expansion based on the Maxwell equations [11]. In this way the nonlinearities of the accelerator optics are included in the slice simulations. The on axis magnetic field input was obtained from the XTR simulation shown in Fig. 1. Transverse magnetic fields from steering dipoles and cell misalignments were input as x, y values that uniformly fill the solution space, an approximation that is obviously best for a beam near the axis. These dipole fields were obtained from XTR, which calculates them on axis from steering dipole excitation currents and cell misalignments, which have been measured [20, 21].

Although the envelope equation only deals with axisymmetric beams centered on axis, the concept of beam emittance is much more general, and it can be calculated for non-axisymmetric distributions in LSP-slice simulations. Consider a non-rotating beam with normalized distribution $\rho\left(x, x'\right)$ in the $\left(x, x'\right)$ plane of phase space. The position of the centroid of this distribution is at

$$\begin{aligned} \langle x \rangle &= \iint x\rho\left(x, x\right) dx dx' \\ \left\langle x' \right\rangle &= \iint x'\rho\left(x, x\right) dx dx'. \end{aligned} \tag{6}$$

Now consider the 2×2 matrix with elements defined by

$$\sigma_{xx} = 4\iint \left(x - \langle x \rangle\right)^2 \rho\left(x, x'\right) dx dx' = 4\left\langle x^2 \right\rangle - 4\langle x \rangle^2$$

$$\begin{aligned} \sigma_{x'x'} &= 4\iint \left(x' - \left\langle x' \right\rangle\right)^2 \rho\left(x, x'\right) dx dx' = 4\left\langle x'^2 \right\rangle - 4\left\langle x' \right\rangle^2 \\ \sigma_{x'x} &= 4\iint \left(x - \langle x \rangle\right)\left(x' - \left\langle x' \right\rangle\right) \rho\left(x, x'\right) dx dx' \\ &= 4\left\langle x x' \right\rangle - 4\langle x \rangle \left\langle x' \right\rangle, \end{aligned} \tag{7}$$

with $\sigma_{xx'} = \sigma_{x'x}$. The sigma matrix for the beam is

$$\sigma_x = \begin{pmatrix} \sigma_{xx} & \sigma_{xx'} \\ \sigma_{x'x} & \sigma_{x'x'} \end{pmatrix}. \tag{8}$$

This matrix is related to the area occupied by the beam in the x, x' cut through phase space by $A_x = \pi\sqrt{\det \sigma_x}$ [22]. Since the emittance is defined as $\varepsilon_{rms} = A/\pi$ in beam optics, it follows that the rms emittance in the x, x' cut through phase space is $\varepsilon_{x,rms} = \sqrt{\det \sigma_x}$. Without loss of generality, one can center the beam in x, x' space, and then from Eq. (7) one gets

$$\varepsilon_{x,rms} = 4\sqrt{\left\langle x^2 \right\rangle \left\langle x'^2 \right\rangle - \langle x x' \rangle^2}, \tag{9}$$

which is again the Lapostolle "4-rms" emittance [13]. Multiplying by $\beta\gamma$ gets the normalized emittance in Eq. (5). The LSP emittance algorithm follows a suggestion by [23], and generalizes this approach to $\varepsilon_{rms} = (\det \sigma)^{1/4}$ [24], where σ is the 4×4 matrix formed from 4D moments as in Eq. (6) and Eq. (7) permuted through all transverse coordinates x, x', y, y'. This convention for ε_{rms} reduces to Eq. (3) for axisymmetric beams.

III. Simulation Results

We based these simulations on the magnetic tune used on the DARHT-II LIA throughout 2013 (Fig. 1). All LSP-Slice runs were initiated just downstream of the BCUZ as shown in Fig. 1. At this location, the beam envelope is a maximum with no convergence, as calculated by envelope and PIC simulations beginning at the diode. Launching the LSP-slice code at such a location has been shown to give the best agreement with full PIC simulations. The beam size is much smaller here than at the diode, which improves the approximations in the codes, and reduces differences between them. This also eliminates errors in LSP-slice that would result from space-charge errors due to different tube size in injector-BCUZ-main LIA. Tube size is constant from here, and higher energy reduces some other differences. Earlier runs suggested $< 20\%$ growth of normalized emittance ε_n at this point.

Magnetic fields on axis that were input to LSP-slice were obtained from XTR, which includes an algorithm for calculating the dipole fields resulting from a table of the measured cell misalignments, as well as the axial field from the focusing solenoids. External electric fields were derived from electrostatic simulations of the accelerating gaps using the locations and voltages for the XTR simulation in Fig.1.

A. Baseline Simulations

For the baseline case corresponding to the tune of Fig 1, a beam concentric with the axis was injected at the launch point shown in Fig. 1. This launch point was chosen because it is an inflection of the beam envelope, which has been shown to produce the best results with the LSP-slice code.

TABLE I

INITIAL BEAM PARAMETERS FOR LSP-SLICE CODE SIMULATIONS.

Parameter	Symbol	Units	Value
Launch Position	z_0	cm	703.11
Axial Magnetic Field	B_{z0}	Gauss	160.6
Envelope Radius	r_0	cm	4.15
Envelope Convergence	r_0'	mr	0.0
Normalized Emittance	ε_n	π-mm-mr	206
Beam Current	I_b	kA	1.68
Kinetic Energy	KE_0	MeV	3.29

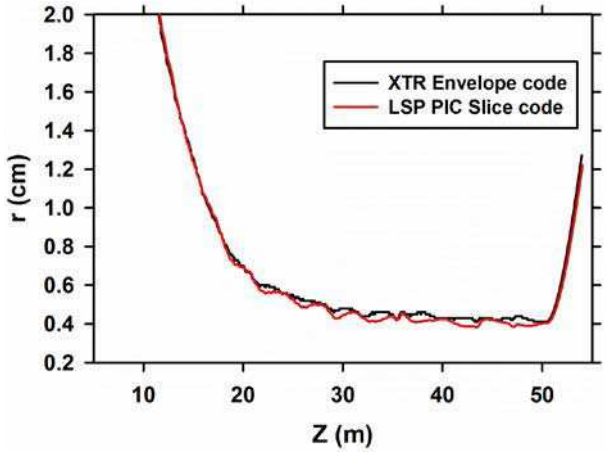

Fig. 2. Beam envelope calculated with XTR and 2D LSP-slice for the tune shown in Fig. 1.

Beam parameters at the launch point were from the envelope code, and are listed in Table I. Figure 2 shows a comparison of results from the XTR envelope code and the LSP-slice code launched with these parameters. Since the LSP-slice output for beam size is the rms radius, this was converted to the equivalent envelope radius vis $r = \sqrt{2}R_{rms}$ whenever necessary.

When comparing results of the LSP-slice code to those of the XTR envelope code, it is well to remember some of the differences in the physics and approximations thereof. Some of these are discussed in the following.

Space charge depression of beam kinetic energy is approximated in XTR by the depression at the beam edge. It is explicit in LSP-slice, including within the beam. XTR approximates space charge depression for variable beam tube size, but tube size in LSP-slice is constant. However, this difference is of little consequence, because for all simulations except those shown in Fig. 3 and Fig. 13, the DARHT tube size is constant.

Beam diamagnetic depression of solenoidal guide field is approximated in XTR. It is explicit in LSP-slice. Different approximations are used by the two codes for the accelerating fields in gap regions.

XTR uses a thin lens approximation for gap focusing. It is explicit in LSP-slice; calculated from electric fields simulated

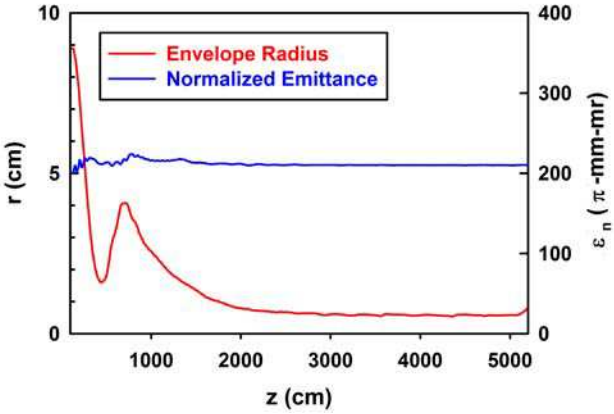

Fig. 3. Envelope radius and normalized emittance ε_n calculated by LSP-slice for the tune shown in Fig. 1.

with the electrostatic code used for Trak. XTR has corrections for image forces at gaps. This is missing in the LSP-slice model.

A rigid rotor with exactly zero canonical angular momentum is assumed in XTR. The rigid rotor in LSP-slice is based on B_z, not rA_θ, so it is less accurate in fringe field regions where B_z varies with r.

The initial emittance at the launch point shown in Fig. 1 was $\varepsilon_n = 206\ \pi$-mm-mr, which was based on PIC-slice code runs beginning at the diode exit, as shown in Fig. 3. There is negligible emittance growth evident in the plot. Since the PIC code includes space-charge depression energy spread, this simulation shows that there is little, if any, growth due to chromatic aberration.

The absence of growth in this simulation is at odds with experimental measurements of emittance at a location after the accelerator exit. These measurements show emittance in excess of $\sim$800 π-mm-mr, so it is important to understand the physical root of this discrepancy. Therefore, we examined the most obvious candidates for growth in turn.

B. Edge Focusing

A well-known contributor to emittance growth in solenoidal focusing systems is spherical aberration [25, 26, 27], which over-focuses the edge of the beam, producing hollow beam profiles. The field expansions used for these simulations include these aberrations, and edge-focusing is noticeable in the PIC simulations. This edge-focusing is a well-known source of emittance growth [27].

Since emittance growth due to spherical aberration of a solenoid lens is proportional to the fourth power of the beam size [27], we design the tunes for DARHT-II to rapidly focus the beam to a small size. Even though the cumulative spherical aberration is noticeable in the baseline simulations (Fig.4) there is apparently little emittance growth ($<\sim$10 π-mm-mr) due to this effect in our baseline simulation (Fig. 3). The effect is mostly due to launching the PIC slice at the diode exit, where the beam is large. Therefore, for the remainder of the simulations, we minimized this effect by launching the slice at the point shown in Fig. 1.

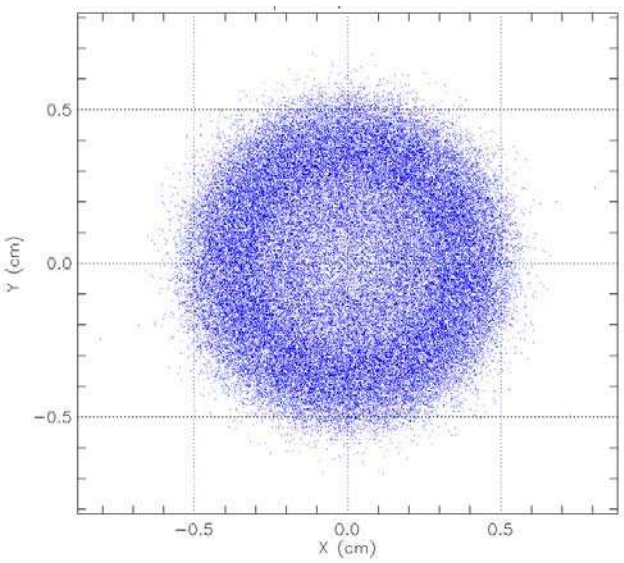

Fig. 4. LSP-Slice particle density in Cartesian coordinates showing the cumulative effect of edge focusing by solenoids from the diode to ∼ 4200 cm (see Fig. 3). This plot has 0.5-cm grid-line spacing.

C. Helical Trajectories

Off center beams can have large helical trajectories in the solenoidal transport field. If the gyro-radius is too large, the beam distribution becomes distorted and the emittance increases. To demonstrate this effect, we initialized the beam for LSP-slice at different values of x_0, adjusting y_0' to produce a helical trajectory of the beam centroid that encircled the axis. Fig. 5 shows the centroid trajectory calculated by LSP-slice for an initial offset of 1 cm, showing how the gyroradius is rapidly focused by the first few solenoids. Fig. 6 shows an end on view of the helical trajectory, and also shows the approximate 2:1 focusing to equilibrium in the LIA. Fig. 7 compares the beam distributions at the exit for several different initial offsets, showing the severe distortion resulting from the largest gyro-radii. Figure 8 shows the emittance growth through the accelerator resulting from the beam distortion for each of these offsets. Obviously, the largest helical trajectories are very dangerous, because of the severe beam distortion and disastrous emittance growth. The results are summarized in Table II. For reference, as measured by our beam position monitors (BPMs) the beam in DARHT-II is within 0.5-cm of the axis through most of the LIA, so emittance growth of more than 10% from this mechanism is not expected.

D. Magnetic Dipole Fields

Another easily identified mechanism for emittance growth is magnetic dipole steering. This is linked to helical motion, since steering with dipoles can cause or correct helical motion of off-center beams. One source of magnetic dipoles in the DARHT-II LIA is cell-to-cell misalignment. Although substantial efforts were made to ensure alignment of the magnetic axis, small misalignments exist (∼0.0 25-mm rms offset, and ∼0.3-mr rms tilt). Beam energy variations coupling with such misalignments is the source of the "corkscrew" motion [28, 29]

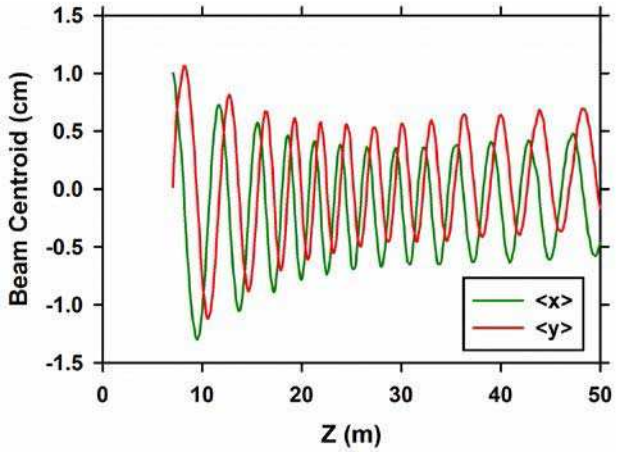

Fig. 5. Trajectory of beam centroid calculated by LSP-slice. The beam was initially injected at $(x_0, y_0) = (1, 0)$ cm. (Green) X coordinate of beam centroid. (Red) Y coordinate of beam centroid

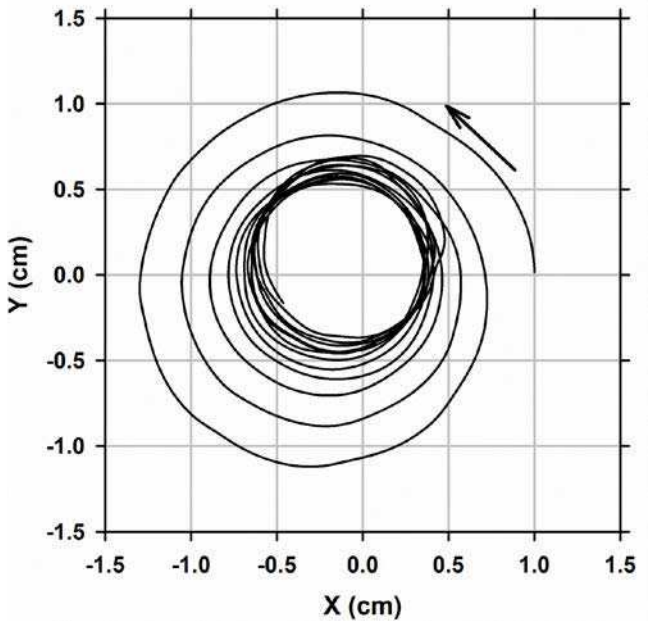

Fig. 6. End on view of trajectory shown in Fig. 5. The direction of motion is indicated by the arrow

TABLE II

EMITTANCE GROWTH FROM LSP-SLICE SIMULATIONS OF BEAMS WITH LARGE HELICAL TRAJECTORIES.

x_0 cm	y_0' mr	Initial gyroradius cm	Equilibrium gyroradius cm	Final emittance π-cm-radian	% Increase over baseline
0.0	0.000	0.0	0.0	0.0190	0
1.0	0.015	1.0	~0.5	0.0197	4
2.0	0.030	2.0	~1.0	0.0225	18
4.0	0.055	4.0	~1.7	0.0399	110
6.0	0.080	6.0	~2.7	0.1884	892

observed in other LIAs [28, 30, 31, 32, 33, 34]. In DARHT-II this interaction causes a slow beam sweep, which is corrected by application of a steering dipole fields at a few locations in

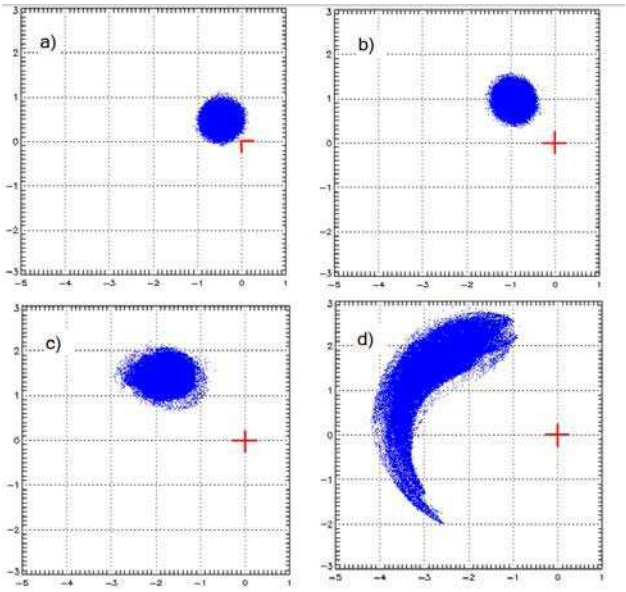

Fig. 7. Distributions for axis-encircling beams at the exit of the LIA. The scales and grids are in 1-cm increments. In all cases the red cross marks the axis of the LIA. a) $(x_0, y_0) = (1, 0)$ cm. b) $(x_0, y_0) = (2, 0)$ cm. c)$(x_0, y_0) = (4, 0)$ cm. d) .These plots all have 1.0-cm grid-line spacing.

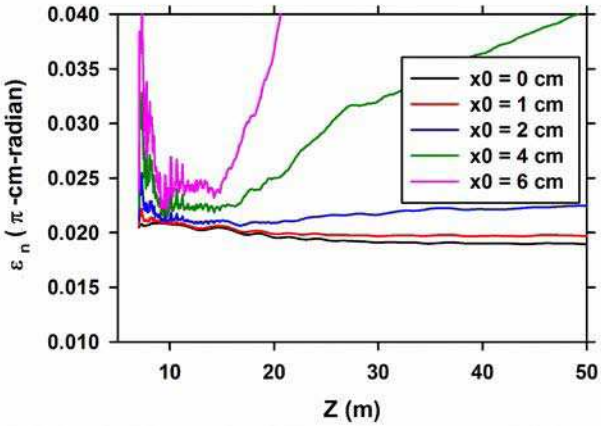

Fig. 8. Normalized emittance growth resulting from axis-encircling beams.

the LIA [4, 5].

The transverse magnetic fields on axis resulting from only the cell misalignments are shown in Fig. 9 for the tune in Fig. 1. These fields were used in an LSP-Slice run to assess the effect of cell misalignment on beam emittance in DARHT-II. As seen in the PIC results in Fig. 10, misalignment fields have essentially no effect on the beam emittance. Moreover, even increasing the misalignment fields by an order of magnitude would only produce a ∼20% emittance growth.

In practice we apply steering dipole fields to correct the beam sweep caused by misalignment fields. Since the transverse fields from the steering coils are an order of magnitude greater than the misalignment fields plotted in Fig. 9 their effect on emittance must be explored. To do this using LSP-Slice, we used the steering dipole fields from an XTR simulation. These were the actual steering fields that we used on the LIA throughout most of 2013. The steering

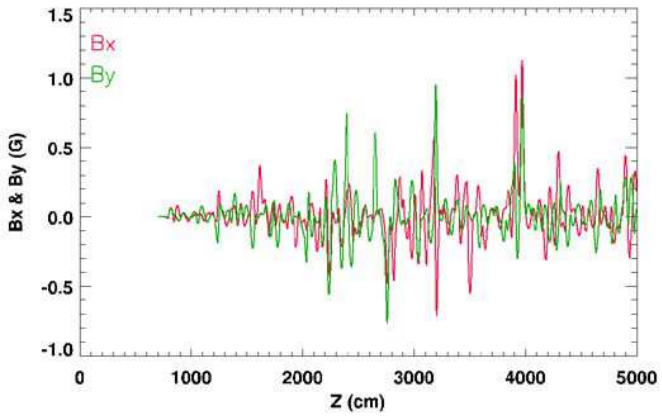

Fig. 9. Transverse magnetic field on axis from measured cell misalignment.

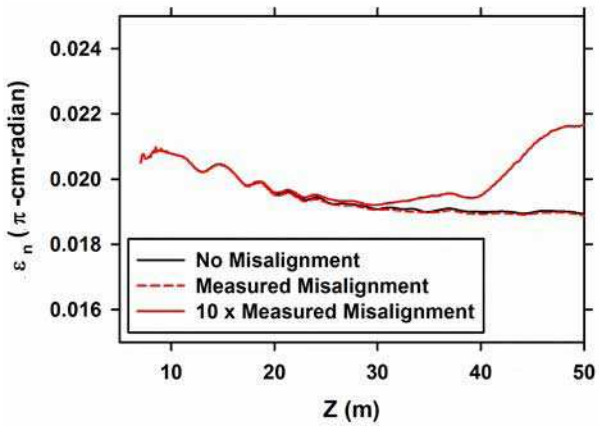

Fig. 10. Normalized emittance growth caused by transverse fields due to misalignment of cells.

fields for these currents are shown in Fig. 11, along with the misalignment fields. The emittance growth caused by the combined misalignment and steering fields is quite small. As shown in Fig. 12 the combined effect of these transverse fields is only a 2.6% emittance increase in the LIA. Therefore, we must look elsewhere for the cause of the discrepancy between theory and observations.

E. Mismatched Beam

Emittance growth can result from envelope oscillations caused by a mismatch of the beam to the magnetic transport system. A badly mismatched beam exhibits large envelope oscillations, sometimes called a “sausage,” “m=0,” or “breathing” mode. The mechanism of this contribution to emittance growth is parametric amplification of electron orbits that resonate with the envelope oscillation, expelling those electrons from the beam core into a halo [35, 36].

Fig. 13 shows the envelope oscillations of a mismatched beam and the resulting emittance growth in an LSP-slice simulation [5]. Halo growth was quite clear in LSP-slice movies of the beam distribution as it propagated through the LIA. Several frames of the movie are displayed in Fig. 14 to illustrate the evolution of the halo in configuration and phase

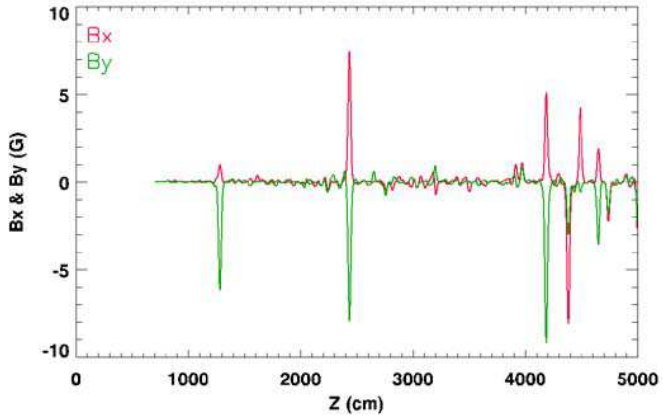

Fig. 11. Transverse magnetic fields on axis from steering dipoles and cell misalignments. Note order of magnitude change of scale from Fig. 9.

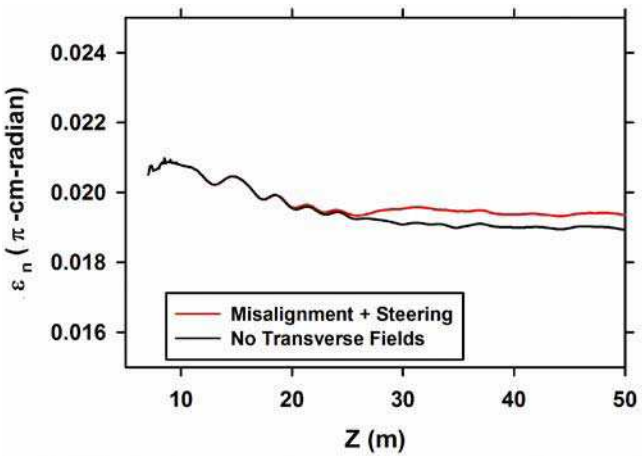

Fig. 12. Normalized emittance growth due to transverse magnetic fields from the combined effects of misalignments and applied steering dipoles

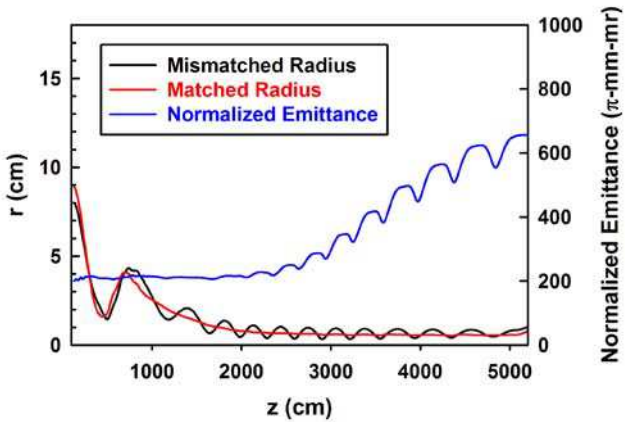

Fig. 13. (Black) Envelope radius of the mismatched beam. (Red) Envelope radius of a matched beam. (Blue) The normalized emittance of the mismatched beam simulated by the 1D version of LSP-slice, showing substantial growth through the LIA. (1000 π-mm-mr=0.10 π-cm-radian) (Adapted from [5])

space.

The slice in this early simulation was launched at the diode exit in order to demonstrate the lack of emittance

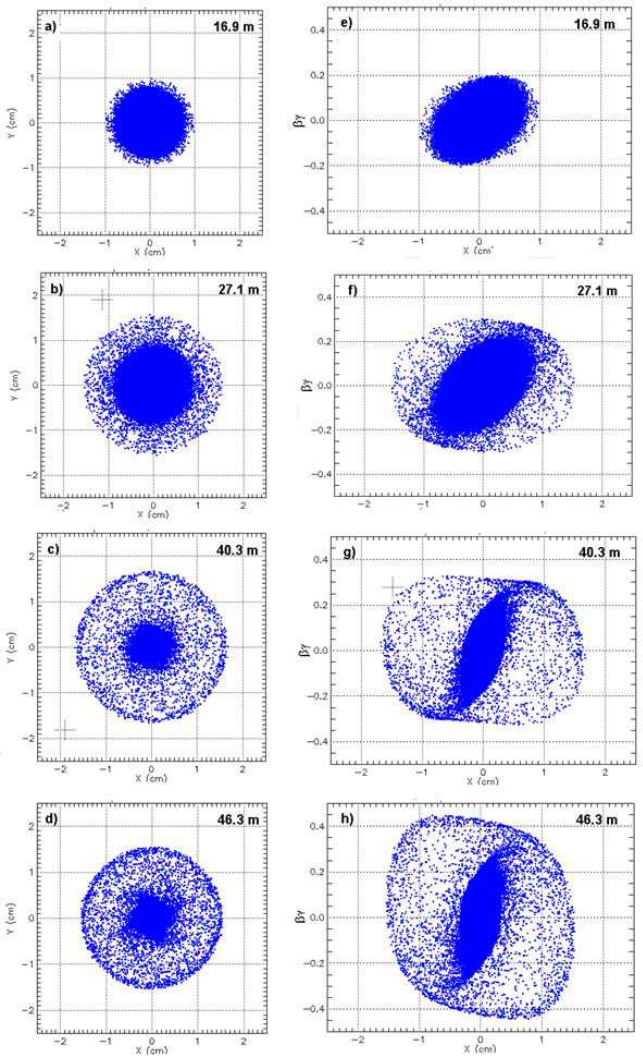

Fig. 14. Left column (a, b, c, d): Configuration space (x, y) showing growth of halo as mismatched beam propagates through LIA (top to bottom). These Cartesian coordinate plots all have 1.0-cm grid-line spacing. Right column (d, e, f, g): Phase space (x, $p_x/m_e c$) showing the increase in phase area (proportional to emittance) as resonant electrons are ejected into the halo. (Adapted from [5]). Phase-space plots have 1.0-cm grid-line spacing on the abscissa, and $\beta_x \gamma = 0.2$ grid-line spacing on the ordinate.

growth in the injector and BCUZ, even though the beam envelope has large amplitude excursions there. In order to directly compare the effect of envelope oscillations with the other effects discussed above, we performed a new series of mismatched beam simulations that were launched at the same point shown in Fig. 1.

Mismatch can be accomplished by varying initial slice parameters from the nominal values given in Table I. Since the initial slice should be launched with $r_0' = 0$, we explored varying either the initial radius or the initial beam energy. Fig. 15 compares the sensitivity of emittance growth from these perturbations in the initial slice parameters. Apparently, they are equally effective for producing the mismatch and emittance growth. However, varying r_0 also affects the beam rotation because it defines the flux required to zero the canonical momentum; $P_\theta = \gamma_0 m_e r_0^2 \omega - e r_0 A_{\theta 0} = 0$, where $A_{\theta 0} \approx$

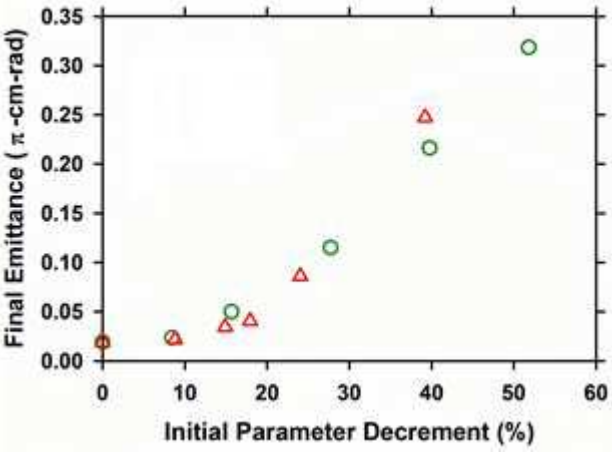

Fig. 15. Comparison of causes of beam mismatch. The final emittance at $z = 52$ m is plotted vs the percentage decrement of the initial radius (green circles) or initial beam energy (red triangles) from their nominal values in Table 1. The 1D version of the code was used for this analysis.

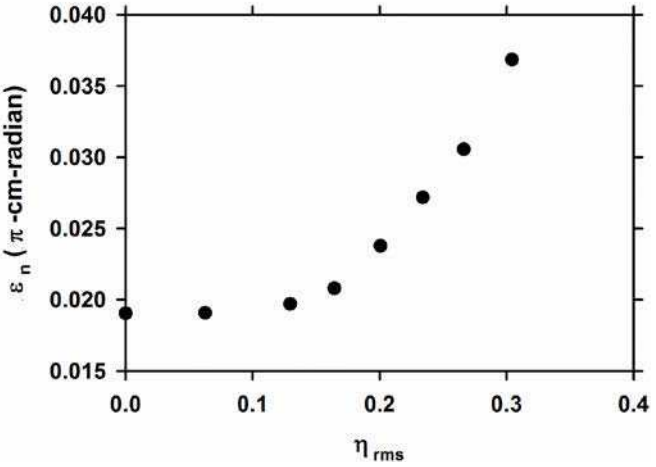

Fig. 16. Final normalized emittance at $z = 52$ m as a function of normalized oscillation amplitude.

$r_0 B_z/2$. Therefore, we only used variations in the initial beam energy to excite the envelope oscillations for this investigation.

Several striking features of this mechanism are evident from the simulation results.

- There is a threshold of oscillation amplitude for emittance growth.
- When the initial envelope oscillations are small, the emittance grows almost linearly
- When the initial envelope oscillations are large, the emittance rapidly grows and then saturates.
- The large halo generated on these severely mismatched beams appears to damp the oscillations after the emittance saturates.
- The most severe cases show evidence of multiple halos.

The envelope oscillation amplitude was defined using the full 2D-Slice data record during the linear phase of the growth. The envelope oscillations were quantified by the amplitude normalized to the size of the matched envelope $\eta = (r - r_m)/r_m$, where r is the mismatched beam envelope and r_m is the matched beam envelope at the same position. Then, the rms value η_{rms} was calculated over four complete cycles of envelope oscillations near the start of observable emittance growth. The final emittance ~1.5 m past the LIA exit at $z = 52$ m is plotted in Fig. 16 as a function of η_{rms}. The onset of emittance growth is evident; with η_{rms} less than ~0.13 the growth is probably not measurable.

The definition of η_{rms} enables a useful means for predicting emittance growth from envelope code calculations. It can be readily calculated from the output of any simulation that produces envelope oscillations, and then used with Fig. 16 to predict the emittance growth that would appear in a full PIC simulation or experiment. For example, XTR simulations of the tune shown in Fig. 1 indicate that increasing the excitation current of the first three solenoids in the second cell block causes noticeable envelope oscillations with $\eta_{rms} = 0.1898$. Inspection of Fig. 17 suggests that the resulting emittance would only be slightly increased to ~0.0230 π-cm-rad.

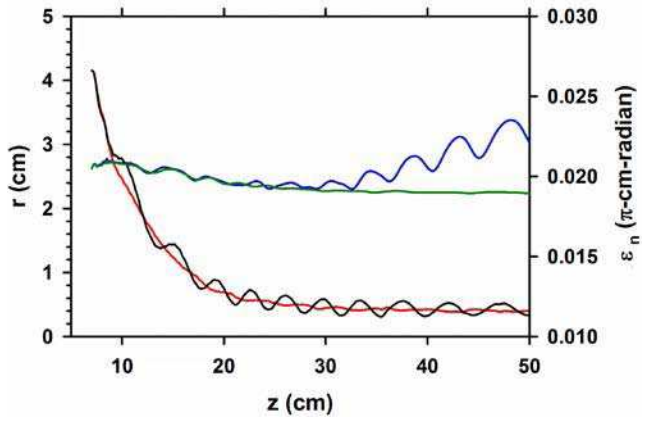

Fig. 17. (Black) Envelope radius of a weakly mismatched beam simulated by the 2D version of LSP-slice. The envelope oscillation normalized amplitude in this simulation is $\eta_{rms} = 0.2$. (Red) Envelope radius of a matched beam. (Green) The normalized emittance of the matched beam. (Blue) The normalized emittance of the mismatched beam, showing linear growth through the LIA.

Linear emittance growth on a weakly mismatched beam is illustrated in Fig. 17. Weakly mismatched beam halos are diffuse, becoming more distinct for worse mismatch and larger envelope oscillations. Rapid emittance growth and saturation on a severely mismatched beam is shown in Fig. 18. Strongly excited halos have one or more distinct rings. The halos of the most severely mismatched beams develop multiple distinct rings, corresponding to higher order resonances. Fig. 19 compares the configuration space distribution just outside the LIA exit for several representative cases of emittance growth, clearly showing multiple rings in the halos of the most severe cases, and diffuse halos for the weak cases. The possibility that the distinct rings in the largest halos result from edge focusing by spherical aberration is yet to be investigated.

That beam halo makes a significant contribution to emittance as calculated by LSP-Slice is easily seen from Eq. (9) and Fig. 20. The emittance is a real physical quantity, independent of the coordinate system in which it is calculated.

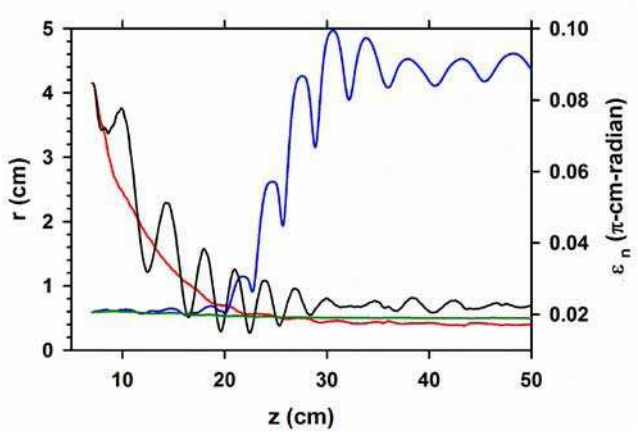

Fig. 18. (Black) Envelope radius of a severely mismatched beam showing damping of the oscillations. The envelope oscillation normalized amplitude in this simulation is $\eta_{rms} = 0.5$. (Red) Envelope radius of a matched beam. (Green) The normalized emittance of the matched beam. (Blue) The normalized emittance of a severely mismatched beam, showing rapid growth and saturation. (Note the emittance scale difference from Fig. 16).

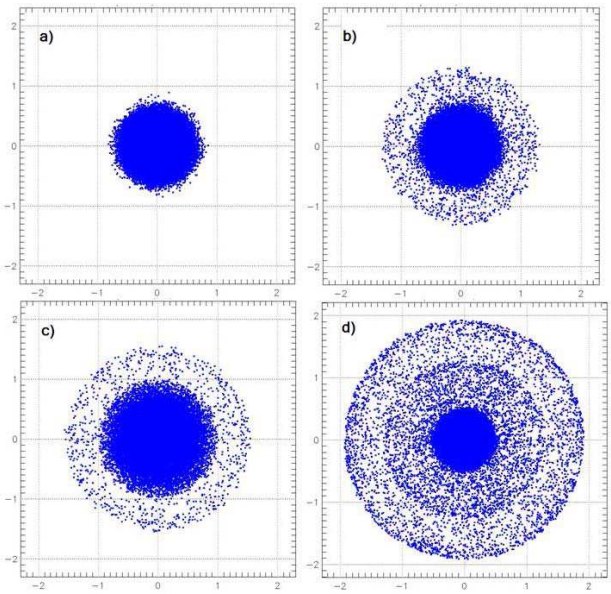

Fig. 19. Beam electron distribution at $z = 52$ m, which is $\sim$1.5 m past the LIA exit. These plots have 1.0-cm grid-line spacing. These plots correspond to the phase space plots in Fig. 20.a) The matched case with $\eta_{rms} = 0.0$, $\varepsilon_n = 0.0191\ \pi$-cm-rad b) The mismatched case shown in Fig. 17 with $\eta_{rms} = 0.2$, $\varepsilon_n = 0.0238\ \pi$-cm-rad c) $\eta_{rms} = 0.3$, $\varepsilon_n = 0.0369\ \pi$-cm-rad d) The severely mismatched case shown in Fig. 18 with $\eta_{rms} = 0.5$, $\varepsilon_n = 0.0901\ \pi$-cm-rad.

The cross-correlation term $\langle xx' \rangle$ in Eq. (9) can be eliminated by an appropriate coordinate rotation. The result in the new coordinate system is $\varepsilon_x = 4\left(\langle x^2 \rangle \langle x'^2 \rangle\right)^{1/2}$ This clearly shows that the emittance is disproportionately affected by particles most distant from the phase-space origin, because of the x^2 and x'^2 weighting. For example, in Fig. 20d, particles at the outer edges of the core and halo contribute equally to the beam current, but the halo-edge particle contributes 3 to 5 times as much to the emittance. Moreover, since the moments are normalized to current, they are proportional to the phase-space area covered by the distribution, suggesting that the halo contributes much more to the emittance than the core for the case illustrated by Fig. 20d.

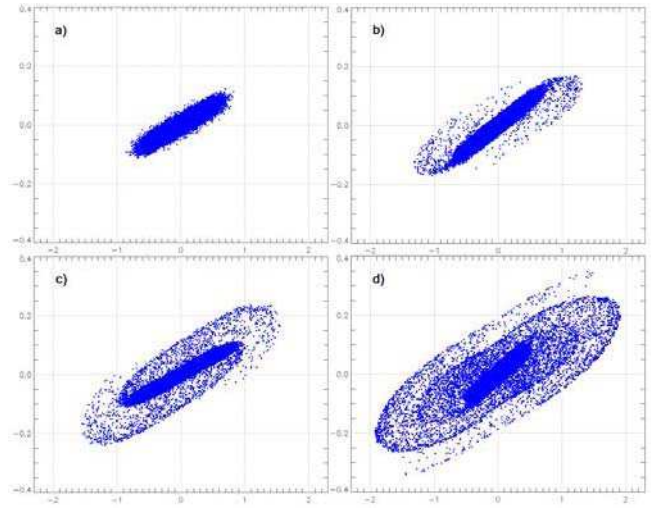

Fig. 20. Phase space plots of the beam distribution at $z = 52$ m, which is $\sim$1.5 m past the LIA exit. These phase-space plots have 1.0-cm grid-line spacing on the abscissa, and $\beta_x \gamma = 0.2$ grid-line spacing on the ordinate. These plots correspond to the configuration space plots in Fig. 19. a) The matched case with $\eta_{rms} = 0.0$, $\varepsilon_n = 0.0191\ \pi$-cm-rad b) The mismatched case shown in Fig. 17 with $\eta_{rms} = 0.2$, $\varepsilon_n = 0.0238\ \pi$-cm-rad c) $\eta_{rms} = 0.3$, $\varepsilon_n = 0.0369\ \pi$-cm-rad d) The severely mismatched case shown in Fig. 18 with $\eta_{rms} = 0.5$, $\varepsilon_n = 0.0901\ \pi$-cm-rad.

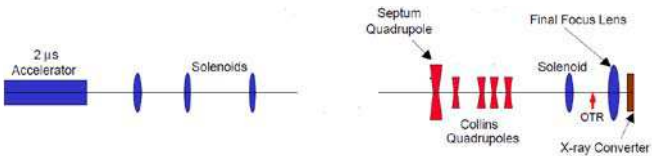

Fig. 21. Magnetic focusing elements of the DARHT-II downstream transport (DST). Imaging of the beam in optical transition light took place at the position labelled "OTR."

Finally, beam halo is especially troublesome for radiography accelerators, such as DARHT, because the wings of the radiographic source spot caused by the halo blurs the image. The effect is as if a low-resolution image due to the halo alone were superimposed on a high-resolution image due to the core. Thus, mismatched-beam generated halo is to be prevented. Since the ideal source-spot size calculated from beam dynamics is directly proportional to emittance, and the emittance is so strongly affected by the halo, the emittance is an effective metric of this radiographic resolution degradation due to halo.

F. Downstream Transport

Finally, because our emittance measurements were made in the downstream transport (DST) section following five quadrupole magnets, we simulated the emittance growth in this region [37]. A simple diagram of the magnetic transport from the accelerator to the bremsstrahlung radiation target is shown in Fig. 21. The initial position of our PIC model was at the third solenoid from the left.

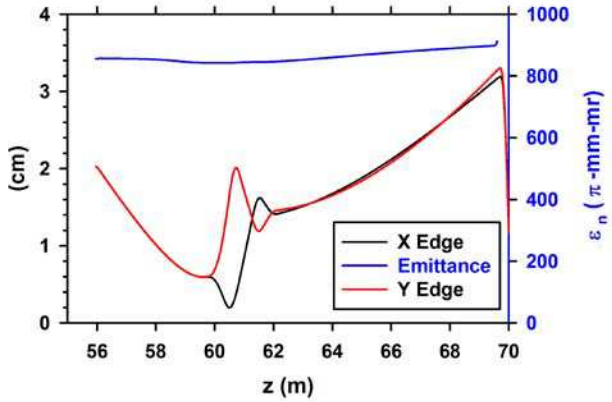

Fig. 22. The x and y edges (envelope projection) are calculated from projections of the distribution. (red) Y edge (cm) (black) X edge (cm). Also shown is the normalized emittance in (blue).

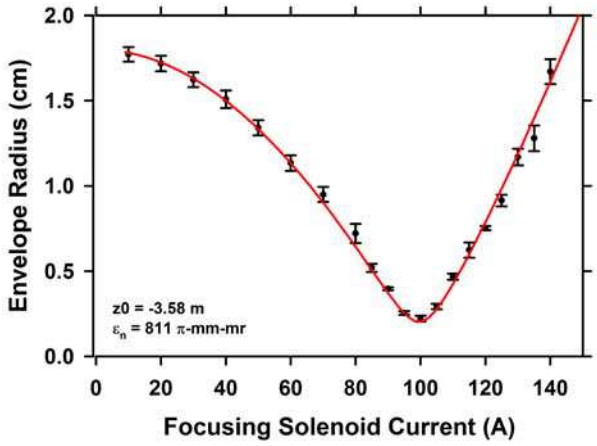

Fig. 23. Beam radius as function of focusing magnet current. Data are from several shots with different magnet currents. The red curve is the best fit by XTR to these data. Error bars indicate uncertainty due to asymmetry of images.

The on axis magnetic field for the solenoids in the DST was calculated from the magnet models used in our LAMDA envelope code, which is used for tuning the DST, because it can simulate beams having elliptical cross-section. These solenoid models are the same as used in XTR, and are based on magnetic field measurements. The magnetic field for the quadrupoles was input as a map derived from the ideal quadrupole equations,

$$B_x(x, y, z) = g(z)y; \;\; B_y(x, y, z) = -g(z)x, \qquad (10)$$

where $g(z)$ is the field gradient. The quadrupole gradients used to generate these maps were taken from the quadrupole models used in LAMDA, which are based on measurements for each of the magnets.

Fig. 22 shows the results from a PIC simulation in which the quadrupole magnet currents were set to obtain a nearly round beam in the post-quad drift region. As seen in Fig. 22, the emittance for this tune is almost constant throughout the DST, with less than 5% growth. Thus, emittance growth in the DST contributes only a small uncertainty to our measurements.

IV. Experimental Results

We estimated the beam emittance with the focal scan technique, in which a single focusing solenoid is used to vary the beam size at a downstream imaging target. An appropriate beam optics code can then be used to find the beam initial conditions at an upstream point by maximum likelihood fitting to the data [38]. In our measurements we used a solenoid 3.8 m upstream of the final focus to change the size of a 50-ns beam pulse produced by the kicker. This solenoid is the fourth from the left shown in Fig. 21. We imaged the optical transition radiation (OTR) from a 51-micron thick Ti target with a 10-ns gated camera. We used the XTR envelope code to fit our data to find the beam envelope size, divergence, and emittance at a position 3.58 m upstream of the focusing solenoid. The data and XTR fit shown in Fig. 23 yielded 811 π-mm-mr normalized emittance. This suggests a severely mismatched beam, such as shown in Fig. 19d.

There are many uncertainties with using this technique. Experimentally, the beam may be defocused by ions produced in beam-target interactions or blurring of the image by motion from the kicker. These sources of error are partially mitigated by using a short imaging gate. There was a strong radiation produced background, which we corrected by subtraction of a "dark field." (Such background subtractions are an obvious source of uncertainty.) Yet another uncertainty results from the asymmetry of the beam (see Fig 24). To mitigate this we used a beam size calculated from the average of projections of the image into 36 different angles. An overlay of these line spread functions (LSF) for the image in Fig. 24 is shown in Fig. 25.

A final comment about asymmetry is that the envelope theory used to fit the data is itself based on an assumption of an azimuthally symmetric beam. That we use this theory to extract information about an asymmetric beam surely contributes an error.

The beam image (Fig. 24) and the overlay of projections (Fig. 25) show clear evidence of beam halo. However, the halo does not appear to be as wide spread relative to the core as in the simulation of a mismatched beam giving approximately the same emittance. Fig. 19d shows the spatial distribution at the LIA exit of a strongly mismatched beam that had an emittance of 901 π-mm-mr; comparable to the measured 811 π-mm-mr. Fig. 25 is the projection of the distribution in Fig. 19d, and here it is seen that the halo in the simulation extends to about 5 beam-core radii, much further than the halo in the data, which only extend to $\sim$3 beam-core radii.

From Fig. 25 we estimate that the halo only contributes $\sim$20% of the beam current, but due to the large radius effect discussed in Section V, it contributes $\sim$50% of the emittance. This is significantly better than the initial measurements on DARHT-II (ca. 2003) reported in [38], when a careful analysis indicated that the halo contributed about 75% of the halo for 20% of the current. As discussed in [38] , emittance filtering with apertures located after the LIA would significantly improve beam quality at the radiographic source spot with little loss of current. Scraping off the halo shown in Fig. 25 might halve the emittance for a loss of only 20% of the beam current.

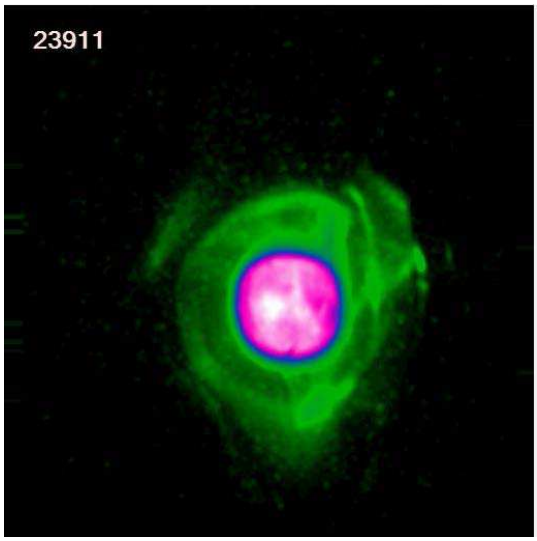

Fig. 24. False color image of one of the spots used for the analysis shown in Fig. 23.

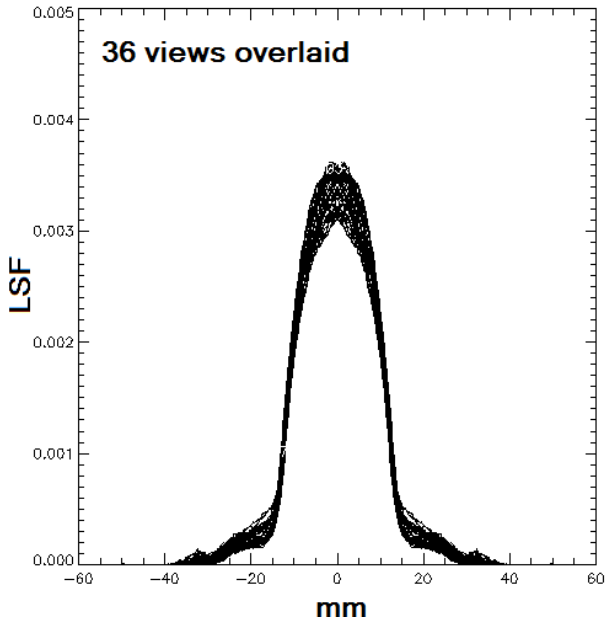

Fig. 25. Overlay of line spread functions (LSF) from projections of the image in Fig. 24 into 36 directions differing by 10 degrees.

V. Conclusion

The DARHT-II beam is centered to less 0.5-cm of the axis at the BPMs throughout most of the accelerator, so it is doubtful that there is much emittance growth caused by large gyro-radius effects. From these simulations, we estimate growth from this cause to be no more than ∼10%, and likely much less.

Emittance growth from the misalignment dipole fields was shown to be insignificant, with a tenfold increase necessary to have a noticeable emittance growth. Moreover, although we apply a number of steering dipoles to correct for beam motion, these simulations show that growth due to steering dipoles in addition to the misalignments is insignificant; $< 3\%$ at most.

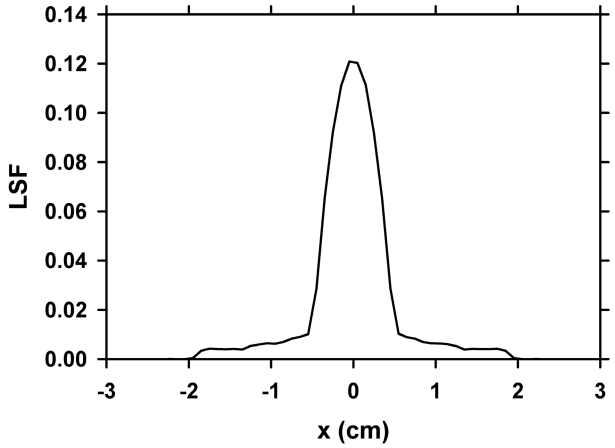

Fig. 26. Projection (Line Spread Function, or LSF) of the beam simulation spatial distribution shown in Fig. 19d.

If growth in the LIA is indeed responsible for the final ∼1000-π-mm-mr emittance, suggested by early measurements, then it is most likely due to envelope oscillations resulting from beam mismatch. Halo growth from the parametric amplification of orbits by the envelope oscillations significantly increased the emittance in these simulations. However, growth to ∼1000 π-mm-mr would only result from a very severe mismatch, with normalized oscillation amplitude $\sim$ 50% or more. This severe a mismatch would indicate that our simulations of initial conditions are grossly inaccurate, possibly because of ion production and neutralization in the BCUZ [39, 40, 41].

Mismatch can result from actual beam initial conditions at the injector being significantly different from the conditions used to design the magnetic tune, which were derived from diode simulations. Furthermore, it is possible that ions generated by beam-head scrape-off in the BCUZ cause partial space-charge neutralization, which would result in a mismatch of the beam to the remainder of the magnetic tune.

The PIC code simulations have shown that improving the beam match to reduce envelope oscillations would reduce emittance growth. The design of our tunes features the ability to improve the match by varying only the first few solenoids after the BCUZ. Since improving the match could reduce the beam envelope oscillations, we are seeking opportunities to use this feature in an attempt to reduce the emittance of the DARHT-II beam.

Acknowledgment

The authors thank their colleagues at Los Alamos National Laboratory, National Security Technologies, and Voss Scientific for many useful and stimulating discussions about beam emittance, beam diagnostics, and related accelerator physics topics.

References

[1] C. Ekdahl, "Modern electron acccelerators for radiography," *IEEE Trans. Plasma Sci.,* vol. 30, no. 1, pp. 254-261, 2002.

[2] K. Peach and C. Ekdahl, "Particle radiography," *Rev. Acc. Sci. Tech.,* vol. 6, pp. 117 - 142, 2013.

[3] J. E. Coleman, D. C. Moir, C. A. Ekdahl, J. B. Johnson, B. T. McCuistian, G. W. Sullivan and M. T. Crawford, "Increasing the intensity of an induction accelerator and reduction of the beam breakup instability," *Phys. Rev. STAB,* vol. 17, no. 3, p. 030101, 2014.

[4] C. Ekdahl, E. O. Abeyta, R. Archuleta, H. Bender, W. Broste, C. Carlson, G. Cook, D. Frayer, J. Harrison, T. Hughes, J. Johnson, E. Jacquez, B. T. McCuistian, N. Montoya, S. Nath, K. Nielsen, C. Rose, M. Schulze, H. V. Smith, C. Thoma and C. Y. Tom, "Suppressing beam motion in a long-pulse linear induction accelerator," *Phys. Rev. ST Accel. Beams,* vol. 14, no. 12, p. 120401, 2011.

[5] C. Ekdahl, "Tuning the DARHT long-pulse linear induction accelerator," *IEEE Trans. Plasma Sci.,* vol. 41, pp. 2774 - 2780, 2013.

[6] M. Schulze and et al., "Commissioning the DARHT-II accelerator downstream transport and target," in *Linear Accelerator Conference (LINAC)*, Victoria, BC, Canada, 2008.

[7] C. Ekdahl, E. O. Abeyta, P. Aragon, R. Archuleta, G. Cook, D. Dalmas, K. Esquibel, R. Gallegos, R. Garnett, J. Harrison, J. Johnson, E. Jacquez, B. T. McCuistian, N. Montoya, S. Nath, K. Nielsen, D. Oro, L. Rowton, M. Sanchez, R. Scarpetti, M. Schauer, G. Seitz, V. Smith, R. Temple, R. Anaya, G. Caporaso, F. Chambers, Y.-J. Chen, S. Falabella, G. Guetlein, B. Raymond, R. Richardson, J. Watson, J. Weir, H. Bender, W. Broste, C. Carlson, D. Frayer, D. Johnson, C. Y. Tom, C. Trainham, J. Williams, B. Prichard, M. Schulze, T. Genoni, T. Hughes and C. Thoma, "Electron beam dynamics in a long-pulse linear induction accelerator," *J. Korean Phys. Soc.,* vol. 59, pp. 3448 - 3452, 2011.

[8] T. P. Hughes, D. C. Moir and P. W. Allison, "Beam injector and transport calculations for ITS," in *Proc. 16th Particle Accel. Conf.*, Dallas TX, USA, 1995.

[9] T. Genoni, T. Hughes and C. Thoma, "Improved envelope and centroid equations for high current beams," in *AIP Conf. Proc.*, 2002.

[10] S. Humphries, Charged Particle Beams, New York: Wiley, 1990.

[11] M. Reiser, Theory and design of charged particle beams, New York. NY: Wiley, 1994.

[12] E. P. Lee and R. K. Cooper, "General envelope equation for cylindrically symmetric charged-particle beams," *Part. Accel.,* vol. 7, pp. 83-95, 1976.

[13] P. M. Lapostolle, "Possible emittance increase through filamentation due to space charge in continuous beams," *IEEE Trans. Nucl. Sci.,* vol. 18, pp. 1101 - 1104, 1971.

[14] S. Humphries, "TRAK: Charged particle tracking in electric and magnetic fields," in *Computational Accelerator Physics*, R. Ryne, Ed., New York, American Institute of Physics, 1994, pp. 597 - 601.

[15] S. Humphries, "Trak Charged Particle Toolkit," Field Precision LLC, 2016. [Online]. Available: www.fieldp.com/trak.html. [Accessed 2016].

[16] T. P. Hughes, R. E. Clark and S. S. Yu, "Three-dimensional calculations for a 4-kA, 3.4 MV, 2 microsecond injector with asymmetric power feed," *Phys. Rev. Special Topics - Accel. Beams,* vol. 2, p. 110401, 1999.

[17] P. Allison, "Beam dynamics equations for XTR," Los Alamos National Laboratory report, LA-UR-01-6585, 2001.

[18] C. Ekdahl, "Noninvasive measurement of electron-beam size with diamagnetic loops," *Rev. Sci. Instrum.,* vol. 72, pp. 2909 - 2914, 2001.

[19] C. Thoma and T. P. Hughes, "A beam-slice algorithm for transport of the DARHT-2 accelerator," in *Part. Acc. Conf.*, 2007.

[20] H. V. Smith and et al., "X and Y offsets of the 18MeV DARHT-2 accelerator components inside the hall," Los Alamos National Laboratory report LA-UR-09-02040, 2009.

[21] H. V. Smith and et al., "X and Y tilts of the 18MeV DARHT-2 accelerator components," Los Alamos National Laboratory report LA-UR-09-03768, 2009.

[22] D. C. Carey, The optics of charged particle beams, New York: Harwood Academic, 1987, p. 99 et eq.

[23] D. Chernin, "Evolution of rms beam envelopes in transport systems with linear x-y coupling," *Part. Accel.,* vol. 24, pp. 29 - 44, 1988.

[24] T. C. Genoni and T. P. Hughes, "Ion-hose instability in a long-pulse linear induction accelerator," *Phys. Rev. - ST Accel. Beams,* vol. 6, no. 4, p. 030401, 2003.

[25] P. Loscialpo, W. Namkung, M. Reiser and J. D. Lawson, "Effects of space charge and lens aberrations in the focusing of an electron beam by a solenoid lens," *J. Appl. Phys.,* vol. 57, no. 1, pp. 10 -17, 1985.

[26] S. Bernal and e. al., "Edge imaging in intense beams," *Phys. Rev. Special Topics - Acc. Beams,* vol. vol. 5, p. 064202, 2002.

[27] V. Kumar, D. Phadte and C. B. Patidar, "A simple formula for emittance growth due to spherical aberration in a solenoid lens," in *Proc. DAE-BRNS Indian Part. Accel. Conf.*, New Delhi, India, 2011.

[28] G. Caporaso, W. A. Barletta, D. L. Birx, R. J. Briggs, Y. P. Chong, A. G. Cole, T. J. Fessenden, R. E. Hester, E. J. Lauer, V. K. Neil, A. C. Paul, D. S. Prono and K. W. Struve, "Beam dynamics in the Advanced Test Accelerator (ATA)," in *5th Int. Conf. High Power Charged Particle Beams*, San Francisco, CA, USA, 1982.

[29] Y.-J. Chen, "Corkscrew modes in linear induction accelerators," *Nucl. Instrum. Methods Phys. Res.,* vol. A292, pp. 455 - 464, 1990.

[30] S. L. Allen, H. R. Brand, F. W. Chambers, Y.-J. Chen, F. E. Coffield, F. E. Deadrick, L. V. Griffith, D. L. Lager, W. J. Mauer, W. E. Nexsen, A. C. Paul, S. Sampayan and W. C. Turner, "Measurements of reduced corkscrew motion in the ETA-II linear induction accelerator," in *Part. Accel. Conf.*, San Francisco, CA, USA, 1991.

[31] Y.-J. Chen, "Control of transverse motion caused by chromatic aberration and misalignments in linear accelerators," *Nucl. Instr. Meth. in Phys. Res. A,* vol. 398, pp. 139 - 146, 1997.

[32] J. T. Weir, J. K. Boyd, Y.-J. Chen, J. C. Cark, D. L. Lager and A. C. Paul, "Improved ETA-II accelerator performance," in *Proc. 18th Particle Accel. Conf.*, New York, NY, USA, 1999.

[33] A. Friedman and et al., "Beam Dynamics in the neutralized drift compression experiment-II, a novel pulse compressing ion accelerator," *Phys. Plasmas,* vol. 17, p. 056704, 2010.

[34] P. A. Seidl and et al., "Short intense ion pulses for materials and warm dense matter research," *Nucl. Instrum. Meth. A,* vol. 800, pp. 98 - 103, 2015.

[35] R. L. Gluckstern, "Analytic model for halo formation in high current ion linacs," *Phys. Rev. Lett.,* vol. 73, pp. 1247 - 1250, 1994.

[36] T. P. Wangler, K. R. Crandall, R. Ryne and T. S. Wang, "Particle-core model for transverse dynamics of beam halo," *Phys. Rev. Special Topics - Acc. Beams,* vol. 1, no. 8, p. 084201, 1998.

[37] C. Ekdahl and M. Schulze, "Emittance growth in the DARHT Axis-II downstream transport," Los Alamos National Laboratory Technical Report, LA-UR-15-22706, 2015.

[38] C. Ekdahl, "Initial electron-beam results from the DARHT-II linear induction accelerator," *IEEE Trans. Plasma Sci.,* vol. 33, pp. 892 - 900, 2005.

[39] T. P. Hughes and et al., "Design of beam cleanup zone for DARHT-2," in *Part. Accel. Conf.*, Chicago, IL, USA, 2001.

[40] T. P. Hughes and H. Davis, "Effect of stimulated and thermal desorption in DARHT-2," in *Part. Accel. Conf.*, 2003.

[41] Y. Tang, T. P. Hughes, C. Ekdahl and M. E. Schulze, "Beam clean-up zone calculations for 2.5 MV, 1.4 kA Experiments on DARHT-2," in *IEEE Pulsed Power Conf.*, 2007.

[42] C. Ekdahl, E. O. Abeyta, H. Bender, W. Broste, C. Carlson, L. Caudill, K. C. D. Chan, Y.-J. Chen, D. Dalmas, G. Durtschi, S. Eversole, S. Eylon, W. Fawley, D. Frayer, R. Gallegos, J. Harrison, E. Henestroza, M. Holzscheiter, T. Houck, T. Hughes, S. Humphries, D. Johnson, J. Johnson, K. Jones, E. Jacquez, B. T. McCuistian, A. Meidinger, N. Montoya, C. Mostrom, K. Moy, K. Nielsen, D. Oro, L. Rodriguez, P. Rodriguez, M. Sanchez, M. Schauer, D. Simmons, H. V. Smith, J. Studebaker, R. Sturgess, G. Sullivan, C. Swinney, R. Temple, C. Y. Tom and S. S. Yu, "Initial electron-beam results from the DARHT-II linear induction accelerator," *IEEE Trans. Plasma Sci.,* vol. 33, no. 2, pp. 892 - 900, 2005.